Terahertz interferometric and synthetic aperture imaging

Aparajita Bandyopadhyay, Andrei Stepanov, Brian Schulkin, Michael D. Federici, Amartya Sengupta, Dale Gary, and John F. Federici

Department of Physics, New Jersey Institute of Technology, Newark, New Jersey 07102

Robert Barat

Otto York Department of Chemical Engineering, New Jersey Institute of Technology, Newark, New Jersey 07102

Zoi-Heleni Michalopoulou

Department of Mathematical Sciences, New Jersey Institute of Technology, Newark, New Jersey 07102

David Zimdars

Picometrix, Inc., 2925 Boardwalk, Ann Arbor, Michigan 48113

Received September 29, 2005; accepted October 24, 2005; posted November 30, 2005 (Doc. ID 65030)

The stand-off imaging properties of a terahertz (THz) interferometric array are examined. For this application, the imaged object is in the near-field region limit of the imaging array. In this region, spherical and circular array architectures can compensate for near-field distortions and increase the field of view and depth of focus. Imaging of THz point sources is emphasized to demonstrate the imaging method and to compare theoretical predictions to experimental performance. © 2006 Optical Society of America

OCIS codes: 280.0280, 280.6730, 110.0110.

1. INTRODUCTION

Over the past several years, there has been an increased interest in the potential of terahertz (THz) imaging. This interest is partially driven by potential applications such as medical imaging, detection and imaging of concealed weapons and explosives, and stand-off detection of chemical and biological agents.[1–3] There are three major factors contributing to this interest:

(a) Terahertz radiation transmits through most nonmetallic and nonpolar media thus enabling THz systems to "see through" concealing barriers such as packaging, corrugated cardboard, walls, clothing, shoes, book bags, pill coatings, etc., in order to probe for concealed or falsified materials.

(b) Many materials of interest for various applications (e.g., explosives, chemical agents, and biological agents for security applications, and pharmaceutical chemicals for online monitoring/control) have characteristic THz spectra that can be used to fingerprint and thereby identify these materials.

(c) Terahertz radiation poses minimal or no health risk either to a person being scanned or the THz system operator.

THz imaging has been rapidly evolving due to advances in THz sources, detectors, and device fabrication methods. The simplest method of THz imaging is the use of a single transmitter and detector, i.e., line-of-sight detection. A reflected[4] or transmitted[5] THz image is obtained on a point-by-point basis by scanning the transmitter/detector pair over the sample under test and recording the THz phase and amplitude at each point. Using this method, THz images of macroscopic objects have been obtained[4,6–9] and extended to THz tomography.[5]

An alternative THz imaging method is to upshift the THz spatial (and spectral) information to visible frequencies.[10] For one such implementation—the electro-optic THz imaging method[11,12]—THz images are shifted into visible light, thus allowing conventional CCD cameras to acquire images at a very rapid rate.

A third class of THz imaging has emerged over the past few years. Called THz synthetic aperture imaging, such methods utilize the measured THz phase and amplitude from multiple positions or from multiple beam paths to reconstruct a THz image. Synthetic aperture imaging methods are widely used in astronomy and radar ranging.[13] Only recently have the various methods been applied to the THz range. Examples of synthetic aperture imaging include synthetic aperture THz impulse imaging,[14] which shares many features with optical holography. In this technique a target is illuminated with pulsed THz radiation. A gated THz receiver records the scattered THz time-domain pulsed waveform from which a frequency-dependent amplitude and phase can be extracted. By measuring the phase of the scattered THz radiation as a function of scattering angle/rotation of the

target, the geometrical shape of the target can be reconstructed.

Other methods of solving the inverse problem of image reconstruction measure scattered THz radiation and use an appropriate wave propagation equation to backpropagate the scattered radiation to reconstruct the scattering object.[15,16] While the previous two examples of synthetic aperture imaging use a finite number of detectors at specific positions to reconstruct THz images, synthetic phased array THz imaging, developed by O'Hara and Grischkowsky,[17–19] utilizes arrayed optical mirrors to reconstruct field-amplitude or energy-density, diffraction-limited THz images. Many individual images can be recorded and superimposed to produce a higher-resolution image.

Rather than using a single detector and multiple mirror orientations as in the synthetic phased array approach, another method of image reconstruction—interferometric imaging—detects the THz electric field at multiple locations and then uses the correlated phase and amplitude of the electric field from various pairs of detectors to reconstruct the image. To apply the interferometric synthetic aperture imaging method to the THz range, the basic technique of radio interferometry[13,20] is employed. Signals at two or more points in space (the aperture plane at which the detectors of the array are located) are brought together with the proper delay and correlated both in phase and quadrature to produce cosine and sine components of the brightness distribution. From the phase delay in wavefront arrival at the sensor positions, the direction and location of the source can be determined.[20] The instantaneous response of an interferometer to point sources can be analyzed by knowing the signal paths.[13]

The imaging interferometer consists of an array of individual detectors or sensors. Each pair of THz detectors measures the amplitude and phase of incoming THz radiation. As a wavefront of THz radiation encounters the array, each pair of detectors measures one spatial Fourier component of the incoming THz radiation as determined by the separation (baseline) of the detector pair. Each spatial Fourier component is represented as a point in the Fourier transform plane (also known as the $u-v$ plane). In order to image the source, additional measurements from other baselines must be carried out. For a given number of detectors N, there are $N(N-1)/2$ possible baseline combinations. An image is generated from the spatial Fourier components of all the different pair combinations. The quality of an image depends on the coverage of the $u-v$ plane, i.e., the number of different points generated in the $u-v$ plane. This in turn depends on the arrangement of the detecting elements of the imaging interferometer array. The primary concern in designing the configuration of detecting antennas is to obtain an efficient coverage of the $u-v$ plane over a range determined by the required angular resolution.

For astronomical applications, the interferometric imaging array is typically operated in the far field. In this limit, any curvature of the incoming wavefronts is negligible. However, for stand-off detection applications, the object to be imaged is typically in the near-field region of the imaging array. Consequently, the far-field image reconstruction[21] must be modified[22] to account for the curvature of the wavefronts in the near field.

To date, THz interferometric imaging and its application to detection of concealed explosives and weapons has been limited to simulations and calculated performance.[3,21,22] In this paper, a continuous wave (cw) THz generation and detection method is used to demonstrate the reconstruction of a THz image using the interferometric technique, and to verify theoretical predictions.

2. THEORY

A. Near-Field versus Far-Field Limits

In order to understand the need for imaging in the near field, consider incoming plane waves (i.e., a point source at infinity) for which the wavefronts are parallel to a plane containing the detector elements of the array [see Fig. 1(a)]. For this configuration, an individual wavefront arrives at all the detectors of a planar array at the same time. For the imaging of a far-field point object (e.g., incoming plane waves), standard Fourier transforms of detector pair correlation produce the reconstructed real im-

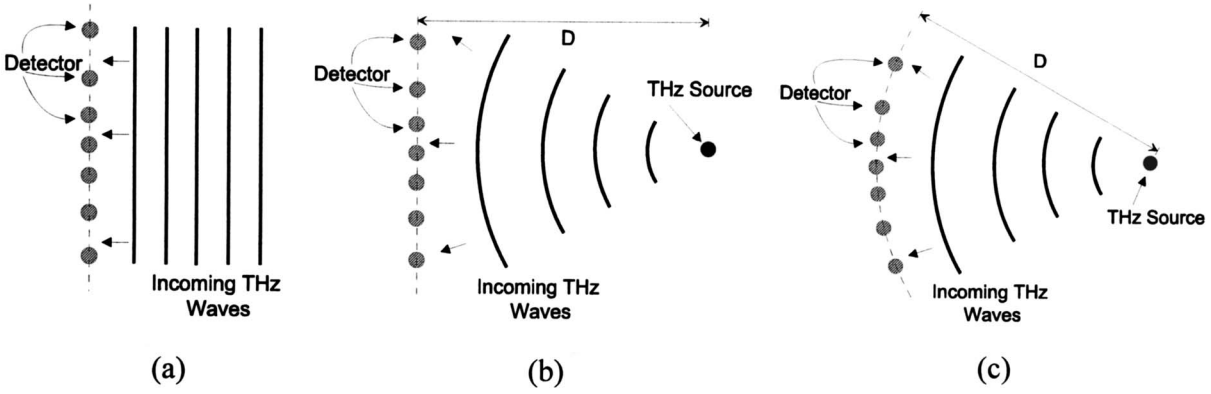

Fig. 1. (a) Parallel wavefronts incident on a planar arrangement of detectors. The wavefront is detected simultaneously at all detectors indicating the presence of a point source at infinite distance from the detection array. (b) For a THz source at finite distance D from the detector array, the wave fronts are curved. There is a phase delay between the different detectors as they sample the wavefront. Since the standard Fourier inversion procedure of interferometric imaging assumes planar wavefronts, the reconstructed image is distorted. (c) By adjusting the placement of the detectors to match the circular wavefronts, the detectors detect the same wavefronts simultaneously. This configuration (a point source at finite distance D) is analogous to a planar arrangement of detectors with the source at infinity [Fig. 1(a)].

age of the object. However, if the point source is located at a finite distance (or is from an extended object), then wavefronts are not planar but curved [see Fig. 1(b)]. If a Fourier transform analysis were performed, the reconstructed image would be distorted because of near-field aberrations.

For a near-field interferometric imaging array, one possible solution to the problem is to match the curvature of the detector array with the curvature of the wavefront. As shown in Fig. 1(c), by placing the detectors on a curved surface, the curvature of the wavefronts and detector array spacing are matched. In this case, an individual wavefront is detected simultaneously by all detectors. This is equivalent to Fig. 1(a) for a point source at infinity. An alternative design, as discussed below, is to minimize the near-field aberrations by arranging the detectors in a circle.

In order to generate images in the near field of the imaging array, in principle the distance to the object must be known so that the curvature of the imaging array can be matched to the curvature of the incoming wavefronts. In essence this corresponds to "focusing" the imaging array on the object. However, this is not a limitation since existing methods (e.g., laser range finders) can be used to determine the distance to the potential target.

B. Synthetic Aperture Imaging Using an Interferometric Array

We introduce the interferometric imaging approach and discuss the required corrections in the near field[22] with a simplified discussion of the Van Cittert–Zernike theorem that relates the interferometric correlation of detector pairs in the imaging array plane to the amplitude of the radiation at the surface of the object.[13,23] A source of radiation localized over an area dS' on the $z=z'$ plane is shown in Fig. 2. ψ_0 is the amplitude of the radiation at source dS'. The source area can be self-illuminating or irradiated from another source of radiation in back or in front of the $x'-y'$ plane. The planar sensor array is entirely in the $x-y$ plane at $z=Z_0$. The contribution to the total electric field from the infinitesimal surface dS' at two detector elements in the sensor array located at (x_1,y_1) and (x_2,y_2) can be expressed as

$$dE_1 = (\psi_0/r_1)\exp(i\omega t - ikr_1)dS', \tag{1}$$

$$dE_2 = (\psi_0/r_2)\exp(i\omega t - ikr_2)dS', \tag{2}$$

where r_1 and r_2 are given by

$$r_j = [(x' - x_j)^2 + (y' - y_j)^2 + {Z_0}^2]^{1/2}. \tag{3}$$

In Eqs. (1) and (2), the electric field is described as a spherical wave whose amplitude is decreasing with propagation distance. In addition, it is assumed that the electric fields are all polarized in the same direction so that the electric fields may be treated as scalar quantities.

For interferometric detection, the correlation of the electric fields at the various pairs of detectors is calculated. It can be shown that the mutual coherence function of the electric fields at points (x_1,y_1) and (x_2,y_2) can be written as[13]

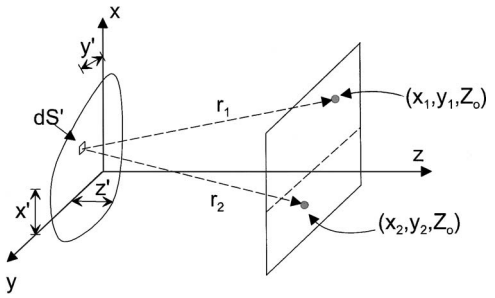

Fig. 2. Source dS' on surface of $z=z'$ plane irradiating a pair of detectors on the imaging array plane located at (x_1,y_1,Z_0) and (x_2,y_1,Z_0).

$$C_{1,2} = \int_S \frac{\sigma_E(x',y')\exp[ik(r_1 - r_2)]}{r_1 r_2} dS', \tag{4}$$

where $\sigma_E(x',y')$ is the time-averaged intensity of the surface at dS', and the integral is taken over the radiating surface S'. This simplified expression also assumes that the electric fields dE from different locations of the surface are uncorrelated (i.e., laser speckle is ignored). This is a valid assumption for the experiments presented in this paper since only point sources are imaged.

Using the expressions in Eq. (3) and assuming $(x'-x)/Z_0 \ll 1$ and $(y'-y)/Z_0 \ll 1$, then $r_1 - r_2$ becomes

$$r_1 - r_2 = \frac{{x_1}^2 - {x_2}^2 + {y_1}^2 - {y_2}^2}{2Z_0} + \frac{(x_2 - x_1)x' + (y_2 - y_1)y'}{Z_0}. \tag{5}$$

By use of the definitions $u=k(x_1-x_2)/2\pi$, $v=k(y_1-y_2)/2\pi$, $\xi=x'/Z_0$, and $\eta=y'/Z_0$ the coherence function of Eq. (4) can be cast in the form[13]

$$C_{1,2}(u,v) = \exp(i\delta)\int_{-\infty}^{\infty}\int_{-\infty}^{\infty} \sigma_E(\xi,\eta)\exp[-i2\pi(u\xi + v\eta)]d\xi d\eta, \tag{6}$$

where the denominator of Eq. (4) has been approximated as $r_1 r_2 \approx {Z_0}^2$.

The phase shift $\delta=k({x_1}^2-{x_2}^2+{y_1}^2-{y_2}^2)/2Z_0$ results from an object in the near field of the planar imaging array. If the object is in the far field ($\delta \ll 1$) such that this phase shift can be neglected, Eq. (6) will then relate the coherence function in the antenna plane to the brightness distribution of the source. By a Fourier transform, the brightness distribution (image) of the source can be reconstructed by measuring the coherence function for a given arrangement of detectors in the sensor array. The condition that the phase shift δ be small can be approximately expressed as $Z_0 \gg b^2/\lambda$ where b is the largest baseline length of the imaging array and λ is the THz wavelength. As will be shown below, this condition cannot be satisfied for imaging of centimeter-size objects that are a few to hundreds of meters from the imaging array.

C. Far-Field Form of Phase Difference between Two Sensor Points in a Planar Array

Two geometric limits are imposed to ensure that the brightness distribution of a source can be imaged through

the coherence function in the antenna plane: In the far field $Z_0 \gg |(x'-x_j)|$, $Z_0 \gg |(y'-y_j)|$, and $Z_0 \gg b^2/\lambda$. The last condition is the most restrictive for stand-off imaging. As an example, assume that a 2.5 cm object needs to be imaged from various distances. The angular resolution of a planar array can be approximated as $\theta_{min}=\lambda/b$. At a distance Z_0 away, the lateral spatial resolution is $\Delta L_{lat} \sim \theta_{min} Z_0 \sim \lambda Z_0/b$. In order to maintain a 2.5 cm lateral spatial resolution at various distances, the maximum baseline for a planar imaging array can be estimated as $b=\lambda Z_0/\Delta L_{lat}$. Using $\delta \sim b^2/Z_0\lambda$ as an estimate of the far-field limit for a planar array, the limit can be estimated as $\delta \sim Z_0\lambda/\Delta L_{lat}{}^2$. Table 1 shows the corresponding maximum baseline required and corresponding phase error. Note that for our application, the far-field criteria of $\delta \ll 1$ is never satisfied, indicating that the imaging from the interferometric array must include the contributions from the near field.

D. Near-Field Imaging with a Spherical or Circular Array

In this subsection, we modify the analysis to correct for the curvature of the wavefronts as present in the near field. Conceptually, we will follow the analogy of Fig. 1(c) and match the curvature of the imaging array to that of the wavefront. Following Fig. 3, we assume that two individual detectors of the spherical imaging array measure an electric field from an element of the surface dS'. For simplicity, we assume that the detectors lie on a spherical surface whose radius of curvature R_0 is centered on the origin. The correlation between the two wavefronts at the two detectors can be calculated from Eq. (4) with r_j expressed in spherical coordinates. One can show that the coherence function becomes[22]

$$C_{1,2} = \exp i\bar{\delta} \int\int \sigma_E(\xi,\eta)\exp(-i2\pi(u\xi+v\eta)\, d\xi d\eta, \quad (7)$$

where $\xi=\bar{x}'/R_0$, $\eta=\bar{y}'/R_0$, $v=k(\bar{y}_1-\bar{y}_2)/2\pi$ and $u=k(\bar{x}_1-\bar{x}_2)/2\pi$. In these expressions, $\bar{x}_2-\bar{x}_1=R_0(\sin\theta_2\cos\phi_2-\sin\theta_1\cos\phi_1)$ and $\bar{y}_2-\bar{y}_1=R_0(\sin\theta_2\sin\phi_2-\sin\theta_1\sin\phi_1)$ are the spherical coordinates of the detectors and the phase error is $\bar{\delta}=kz'(\cos\theta_2-\cos\theta_1)$.

If the near-field phase error $\bar{\delta}$ can be neglected, Eq. (7) would then relate the coherence function to the brightness distribution of the source. Assuming that the azimuthal angles of the detectors are not equal, the magnitude of the phase error can be calculated assuming that the largest azimuthal angle is determined by the distance to the object and the largest baseline distance. For the baseline and distances listed in Table 1, the largest value of $\cos\theta_2-\cos\theta_1 \approx 7.2\times10^{-5}$ independent of the distance to the object. If $\bar{\delta}=1$, the approximate depth of focus (range of z') can be estimated as that for which the phase errors are small and the object is in focus in the near field. For a frequency of 1 THz, the depth of focus would be ±0.7 m.

An alternative configuration that eliminates the phase error is to arrange the detectors in a circle. In this configuration, all detectors have the same azimuthal angle thereby enforcing $\bar{\delta}=kz'(\cos\theta_2-\cos\theta_1)=0$. For this circular arrangement, the first-order phase error vanishes, implying a much larger depth of focus.

The form of the coherence function of a near-field imaging array approaches the far-field planar array limit when $R_0\to\infty$, since at very large radii of curvature, the surface of the spherical array now becomes flat. When $R_0\to\infty$, $\exp i\delta=\exp ikz'(\cos\varphi_2-\cos\varphi_1)\to1$ since the azimuthal angles are virtually zero. As $Z_0\to\infty$, $\exp i\delta=\exp ikb^2/Z_0\to1$.

Table 1. Estimated Phase Error δ in Imaging a 2.5 cm Object at Various Distances Using 1 THz Radiation

Z_0 (m)	5	10	50	100	500	1000
b (m)	0.06	0.12	0.6	1.2	6	12
δ	2.4	4.8	24	48	240	480

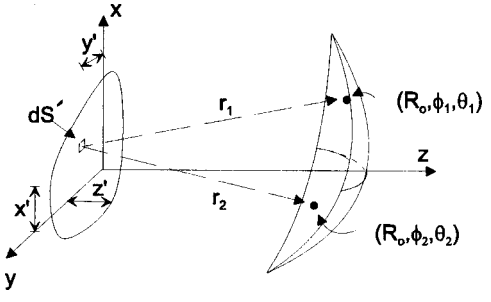

Fig. 3. Element of surface dS' producing wavefronts at two points on the surface of a spherical array. The detectors are located at spherical coordinates (R_0,ϕ_1,θ_1) and (R_0,ϕ_2,θ_2). (R_0,ϕ_1,θ_1) denote the distance from the point to the origin, the angle relative to the x axis in the x–y plane, and the angle relative to the z axis, respectively.

3. EXPERIMENTAL CONFIGURATION

A. Terahertz Photo-Mixing System

To demonstrate THz image reconstruction using interferometric imaging, a cw THz generation and detection method is employed. Continuous wave (cw) generation of THz radiation by photo-mixing has a long history. Generation of cw THz radiation by photo-mixing (beating) of two infrared laser sources commenced in the 1990s with the seminal work of McIntosh *et al.*[24] and Duffy *et al.*[25] The technology for growth, design, and characterization of low-temperature (LT)-grown GaAs photomixers has improved dramatically,[24,25] thus enabling the use of cw THz systems for sensing, spectroscopy,[26,27] and imaging applications.[28–32] The key materials component of LT GaAs and higher power ErAs:GaAs photo-mixers is the presence of nanoparticulates that reduce the charge carrier lifetime in the material to the subpicosecond level, thereby enabling optical mixing to the THz range. While there have been improvements in photo-mixer performance with ErAs:GaAs materials,[33] the photo-mixer approach has been limited by the achievable output power and device reliability.[34] To circumvent the carrier lifetime

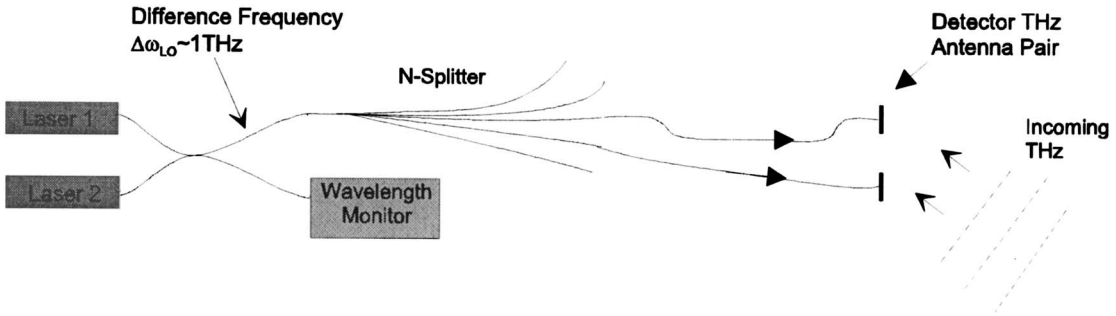

Fig. 4. Schematic representation of interferometric imaging array receiver. Two infrared lasers power the THz photo-mixer receivers through fiber-optic cables.

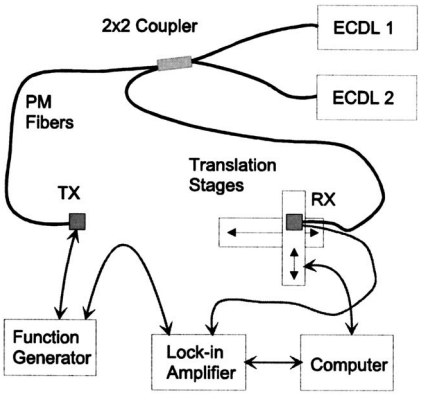

Fig. 5. Schematic diagram of cw photo-mixing apparatus.

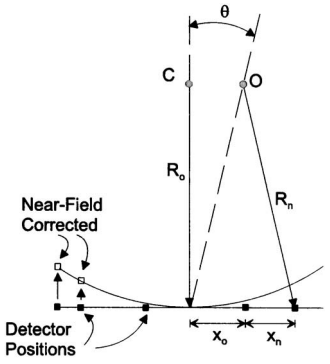

Fig. 6. Geometry and location of detector array positions (solid squares) and source location (point O at an angle of θ) for near-field correction. For the near-field correction, the appropriate phase is added to the measured THz phase such that the position of the detectors is moved from the line of solid squares to positions (open squares) along the curved path. The radius of curvature of the curved path is R_0. The distance from the source to each detector position (x_n) is given by R_n. The value of x_0 represents distance from the $x_n=0$ detector to the origin.

limits of the GaAs system, several groups have utilized *p-i-n* photodiode structures.[34] Terahertz photo-mixing by resonant excitation of plasma oscillations in quantum well structures has also been considered.[35,36] While the GaAs system uses infrared lasers at ~800 nm wavelengths, the InAlAs/InGaAs system can utilize inexpensive telecommunications lasers operating near 1.5 μm.[37] In addition to semiconductor based systems, cw THz generation and detection has been demonstrated using nonlinear optical crystals.[38]

A conceptual diagram of the receiving array is shown in Fig. 4. Two infrared lasers are tuned to have a difference frequency of ~1 THz to power the fiber-optically coupled THz photo-mixer receivers. Because of the relatively low power requirements of the receiver, the optical power from a single set of lasers can be distributed using a fiber-optic splitter to power each element of the imaging array. The receiving array is tunable by simply adjusting the difference frequency of the infrared lasers.

The experimental system that is used to demonstrate the concept of interferometric imaging in the THz range is shown in Fig. 5. In advance of the availability of multiple THz detectors for a complete *N*-element detector array (Fig. 4), we use a single homodyne detector at multiple positions to sample the phase and amplitude of the wavefront from a pointlike THz source. The electric field correlation can then be calculated for each "pair" of detector positions, thereby mimicking the performance of an *N*-element detector array. That information is used to test the near-field imaging performance and techniques expected for an interferometric array. The relative reference phase for each "detector" remains fixed since the infrared signals are delivered to the receiver (Rx) via a fixed-length fiber pigtail.

Two external cavity diode lasers (ECDL) in the Littrow configuration are used as the infrared laser sources. The ECDL lasers can be electronically tuned from 778 to 782 nm. The linewidth of each laser is ~2 MHz with an output power of ~100 mW. The lasers are very sensitive to feedback. Consequently, an optical isolator is utilized to prevent backreflections into the laser cavity. In addition, the fiber launch assembly is designed such that the backreflection from the fiber front surface does not come back into the laser cavity. Since the photo-mixing process requires that the electric fields of the optical sources be collinear, polarization-maintaining fiber is used to deliver the optical power to the fiber-pigtailed THz transmitter (Tx) and Rx.[6] A 2×2 fiber coupler is used to combine the infrared laser beams into fibers for delivery to the THz Tx and Rx modules. The Tx and Rx modules are LT-grown, GaAs bowtie-type photo-mixers. The Tx emits radiation when a voltage bias is applied to the LT-GaAs in the presence of the two infrared beams. The Rx generates a voltage in the presence of the infrared beams that is proportional to the THz electric field. The THz radiation is emitted within a 30° angle[39] using a hy-

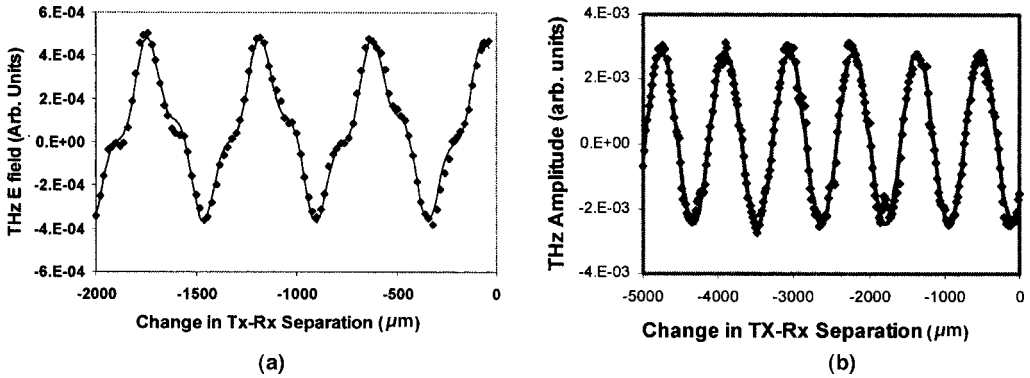

Fig. 7. (a) Homodyne waveform as acquired by changing the separation between the Tx and Rx in Fig. 5. The solid curve shows a numerical fit to the data. The fundamental extracted frequency, 0.535 THz, compares well with the expected frequency based on the frequency difference of the two ECDL lasers. The extracted E field amplitudes and phases are 3.37×10^{-4} and 2.17 radians for 0.535 THz and 5.61×10^{-5} and 3.94 radians for the 1.605 THz third harmonic, respectively. (b) A similar waveform is obtained with an ECDL difference frequency of 0.354 THz.

perhemispheric lens that is attached to the THz module. Based on previous measurements,[38] one would expect the THz radiation at ~0.5 THz to be emitted as a spherical wavefront corresponding to a pointlike THz source.

The cw THz radiation is generated by tuning the difference frequency of the ECDL lasers to approximately 0.5 THz. The amplitude of the THz radiation is chopped at 100 kHz by modulating the electronic bias to the THz Tx. The modulated THz electric field is detected by using a lock-in amplifier. The location of the THz Rx is positioned by two translation stages. One stage, which translates the Rx toward the receiver, is used to measure the phase and amplitude of the THz electric field. The second stage, which translates the Rx laterally, is used to position the Rx at different locations corresponding to different "detectors" in the interferometric imaging array. The initial spacing between the Rx and Tx is approximately 14 cm.

The geometry and location of the Tx relative to the array detector positions is shown in Fig. 6. Point O is the location of the THz source that makes an angle θ relative to the normal to the linear array of detectors. The position of the N detectors is given by x_n while x_0 represents the offset of the $x_n=0$ detector position from the origin. For the values of R_0 investigated, the variation in the measured THz amplitude in a linear (solid squares) compared with curved geometry (open squares) is rather small. The predominant effect on the THz electric field is the additional change in phase from positioning the detectors on the linear compared to curved geometry. For small angles θ, the phase change is given by

$$\phi = k(R - \sqrt{(R_0 \tan\theta)^2 + R_0^2}) + \phi_{off}, \tag{8}$$

where $R=\sqrt{(x_0+x_n-R_0\tan\theta)^2+R_0^2}$ and ϕ_{off} represents a constant offset phase.

B. Generation of Homodyne Waveform

The configuration of Fig. 5 is commonly referred to as homodyne. The homodyne waveform is determined by recording the THz electric field as a function of separation between the Tx and Rx. (A negative value for the separation corresponds to a decreasing distance between the Tx and Rx.) Displacement of the detector to N different positions in the transverse direction will simulate an N-element detector array. Figure 7 shows a typical measured homodyne waveform and corresponding numerical fit. The measured THz waveform exhibits both the fundamental ECDL difference frequency as well as higher harmonics—predominantly the third harmonic. Multiple harmonic generation in THz photo-mixers has been previously reported.[40] By fitting Fig. 7(a) to a sum of harmonic sinusoidal functions, the amplitude and phase of the THz electric field can be determined separately for the fundamental and third harmonic. By tuning the difference frequency of the two ECDL lasers, one can alter the fundamental frequency of the THz wave [see Fig. 7(b)].

4. RECONSTRUCTION OF THE TERAHERTZ IMAGE

Unlike focal-plane-array imaging, for which the individual detectors are typically spaced at regular intervals, interferometric imaging is most effective for an aperiodic detector spacing that is nonredundant. At each detector position, a homodyne waveform is recorded and the THz amplitude, phase, and frequency extracted from a numerical fit to the data. Since the homodyne waveform is periodic over 2π, multiples of 2π can be added to the measured phase to "unwrap" its value. The detector positions that are used in the experiment are given by the formula $x_n=0.0125(1.7^n-1.7^6)$ where x is in units of centimeters, and $n=0,1,\ldots,7$ is the corresponding label for each detector position. The $n=6$ detector position, which is roughly in the geometric middle of the array, is chosen to be at $x=0$. The effective distance between the Tx and Rx is $Z_0\sim14$ cm.

Figure 8 shows the measured THz phase and amplitude compared to theoretical predictions. The left-hand panel compares the measured THz amplitude to that expected for a point source at $R_0=14.4$ cm. The measured THz amplitudes fall just below this line, as is expected since the Tx is known to emit a peak THz electric field along the optical axis.[39] The right-hand panel compares the "unwrapped" measured phase to the expected phase for a point source emitting spherical wavefronts a distance R_0 from the Rx. The solid curve is a theoretical fit to

the measured phase using Eq. (8). Clearly, the incoming wavefronts, based in particular on the measured phase, are curved rather than planar (for which the phase would be constant). Therefore one might expect some near-field distortions to the reconstructed image, particularly if the detector positions exceed a ~5 mm baseline.

Ignoring any near-field correction, we reconstruct[3,21,22] the THz line image from Eq. (6) using the following formulas:

$$\sigma_E(\xi) = \sum_{i=1}^{N(N-1)/2} \{\mathrm{Re}[C(u_i)]\cos(2\pi u_i \xi) - \mathrm{Im}[C(u_i)]\sin(2\pi u_i \xi)\}, \quad (9)$$

$$u_i = \frac{(x_n - x_m)}{\lambda}, \quad (10)$$

where σ_E is the brighness distribution (image), $\xi = x/Z_0$, x_n and x_m are the detector positions, and the iteration of n and m is chosen such that each baseline combination [of the $N(N-1)/2$ possible] is included. $C(u_i)$ is the correlation function given by

$$C(u_i) = A_i e^{i\Delta\phi_i}, \quad (11)$$

where $A_i = E_n E_m$ and $\Delta\phi_i = \phi_n - \phi_m$ represent the product of the electric field amplitudes and change in phase for each baseline pair combination, respectively. The summation over i includes in the reconstructed image the contribution from each spatial Fourier component corresponding to each unique baseline separation. The above equations represent the simplest reconstruction of the image: The correlation function for each possible *unmeasured* baseline pair combination is assumed to be zero.

The reconstructed 0.535 THz image of the Tx point source is shown in Fig. 9(a). In essence the THz image is a measure of the array's point spread function. Note that the reconstructed image closely resembles that of a point source. Since the largest baseline is small compared to the distance to the source, the phase of the wavefront varies only slightly across the detector array. Consequently, near-field corrections to the reconstructed image would be small. From theoretical considerations,[21,22] the angular resolution of a planar array can be approximated as $\theta_{min} = \lambda/b$. At a distance R_0 away, the lateral spatial resolution is $\Delta L_{lat} \sim \theta_{min} R_0 \sim \lambda R_0/b$. For the maximum baseline value $b = 5$ mm used in this experiment, the angular resolution is estimated to be 6.4°. Note that the FWHM for

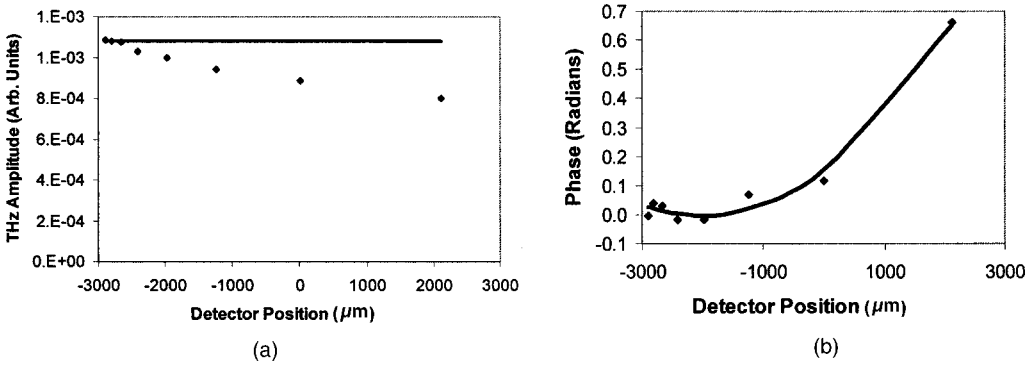

Fig. 8. Symbols represent the data that are extracted from the homodyne waveforms (e.g., Fig. 7). The solid curves are theoretical values assuming that the source is a point source located at R_0 (i.e., incoming spherical waves of constant amplitude). (a) The measured THz amplitude as a function of lateral detector position. (b) The measured phase as a function of lateral detector position. The extracted parameters from Eq. (8) for R_0, x_0, θ, and ϕ_{off} are 14.4 cm, 0.275 cm, 0.29°, and 3.38 radians, respectively.

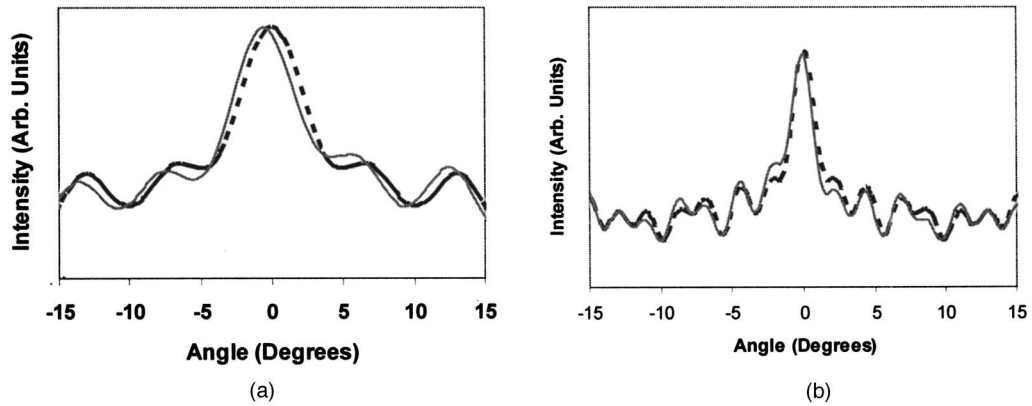

Fig. 9. (a) Reconstructed image of 0.535 THz source located directly in front of the detector a distance of 14.4 cm away. The dashed curve is the expected image reconstruction assuming a point source at infinity (FWHM=4.8°). (b) Similar reconstructed image for 1.602 THz. Note that the resolution of the central peak FWHM=1.6° is improved by a factor of three corresponding to a 1/3 reduction in the THz wavelength.

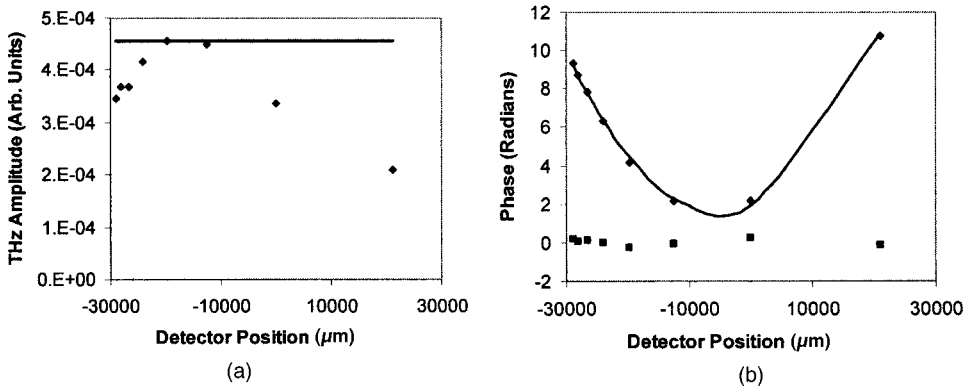

Fig. 10. Measured THz amplitude (a) and phase (b) as a function of lateral detector position in the imaging array. The measured THz phase (diamonds) can be well fitted (solid curve) assuming a point source. The extracted parameters from Eq. (8) for R_0, x_0, θ, and ϕ_{off} are 40.9 cm, 0.520 cm, 0.01°, and 1.55 radians, respectively. The curvature of the phase (b) is indicative of spherical THz wavefronts. The corrected phase (measured minus theoretical fit) is indicated by squares.

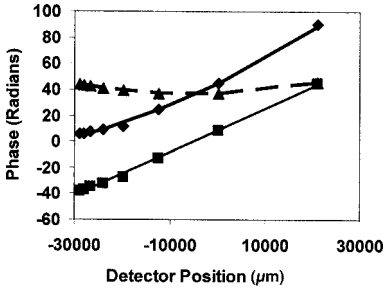

Fig. 11. Similar figure to Fig. 10(b). The diamonds are the unwrapped phases extracted from the homodyne waveforms. The curvature of the data is indicative of a curved wavefront while the tilted slope is indicative of an inclined wavefront. The triangles represent the near-field correction [from Figure 10(b)]. The squares represent the near-field corrected phase. The curvature of the phase as a function of lateral detector position has been removed by the near-field correction.

the reconstructed image (4.8°) is close to this value, indicating a good correspondence between the reconstructed image and theoretical predictions.

A reconstruction of the (third harmonic) 1.6 THz image [see Fig. 9(b)] shows a narrowing of the central peak to a FWHM of 1.6° corresponding to a factor of 3 reduction compared with Fig. 9(a). This is consistent with the expected 1/3 reduction due to the third harmonic of the THz wavelength. Previous analyses of THz interferometric images show that the wavelength-dependent spatial resolution may lead to spectral misidentification of the object boundaries.[3]

While the experimental data match well with what one would expect for a point THz source, the 4.8° angular resolution is not adequate for stand-off applications. In order to improve angular resolution, one must increase the maximum baseline of the imaging array. However, one would expect larger near-field distortions in the reconstructed THz image since (a) wavefront curvature will be more evident and (b) the value of the THz E field [Fig. 8(a)] is not nearly constant along a spherical wavefront but rather exhibits the THz transmitter's 30° divergence angle with peak intensity along the optical axis.[39]

To demonstrate improved spatial resolution, the detector positions in the imaging "array" are scaled by a factor of ten:

$$x_n = 0.125(1.7^n - 1.7^6). \tag{12}$$

The corresponding minimum and maximum baseline values are ~875 μm and ~5 cm, respectively. The initial distance to the point source is R_0=40.9 cm. Figure 10 shows the measured THz amplitude and phase as a function of detector position. The solid line in the amplitude plot corresponds to the expected value for an "ideal" THz point source at R_0=40.9 cm. The decreasing THz amplitude as one moves away from the THz beam center is more prominent. Compared with Fig. 8, the measured THz phase and amplitude show a much more pronounced change in phase as a function of detector position, indicating a curved wavefront.

In order to check that the detected phase is indeed sensitive to the direction of the wavefront, the measurement was repeated for a point source displaced $\theta \sim -6°$ from the center axis of the imaging array. As shown in Fig. 11, the curvature of the phase that is related to the curvature of the wavefront remains while the overall phase is inclined, indicative of the −6° displacement of the source.

The data of Fig. 10 are used to reconstruct a line THz image. Figure 12(a) is a comparison of the reconstructed line image using Eq. (9) (no near-field correction) with theoretical predictions for a point at infinity (i.e., planar wavefronts). When the image is not corrected for near-field distortions (i.e., the spherical wavefronts), there is very poor agreement between the reconstructed image and the theoretical prediction. However, when the near-field corrections are included in the image reconstruction [Fig. 12(b)], the agreement is greatly improved. The smaller peaks at ~±8° and ~±14° are called sidelobes. They are an artifact of the image reconstruction process and the finite number of sampled baselines.

The near-field correction is calculated conceptually by repositioning the detector positions from a linear arrangement [Fig. 1(b)] to a spherical arrangement that matches the curvature of the incoming wavefront [Fig. 1(c)]. As shown in Fig. 10(b) and Fig. 11, the theoretical phase delay from a point source at normal incidence is subtracted from the measured phase. As shown in those figures, the curvature of the phase (indicating a curved wavefront) is removed by the near-field correction yielding a linear dependence of phase on detector position. The slopes of the

near-field corrected phase versus detector position plots indicate the direction to the source.

Figure 13 shows the comparison of the reconstructed image with near-field correction to what one would theoretically expect from a point source. For an ideal point source, both the phase and amplitude of the THz radiation should be constant across the spherical wavefront. A comparison of the ideal point source image to the experimental data [Fig. 13(a)] shows good, but not exact agreement. If instead, only the phase of the near-field source is corrected and then used together with the experimental data for the THz amplitude (i.e., not constant across the wavefront), the agreement with theory and experimental data is improved [Fig. 13(b)]. This suggests that while the near-field correction to the THz phase is effective, we must also correct for the THz beam intensity profile from the THz Tx.

The reconstruction of the point source shifted −6° from normal incidence is shown in Fig. 14. As with Fig. 12(a), the reconstructed image from uncorrected data [Fig. 14(a)] does not match the theoretical prediction for a point source at −6°. However, when the same near-field correction that is applied to the 0° data [Fig. 12(a)] is applied to the −6° data, the reconstructed image [Fig. 14(b)] agrees well with the theoretical expectation.

5. CONCLUSIONS

The imaging properties of a THz interferometric imaging array are examined in the context of stand-off THz imaging. The presented data and the reconstructed images are, to our knowledge, the first experimental demonstration of interferometric imaging in the THz range. For typical target distances and required angular resolutions

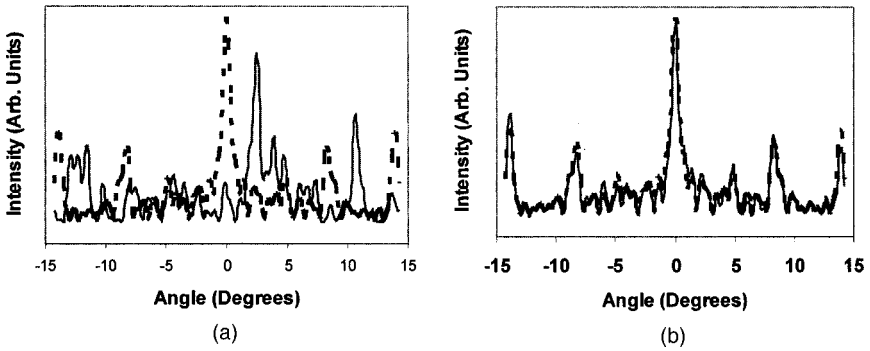

Fig. 12. (a) Comparison of a reconstructed line image (solid curve) without near-field correction and theoretical image (dashed curve) for a point source at infinity. (b) Comparison of reconstructed line image (solid curve) including a near-field correction. The measured FWHM of 0.6° is about an order of magnitude smaller than in Fig. 9(a) corresponding to a factor of 10 increase in the largest baseline.

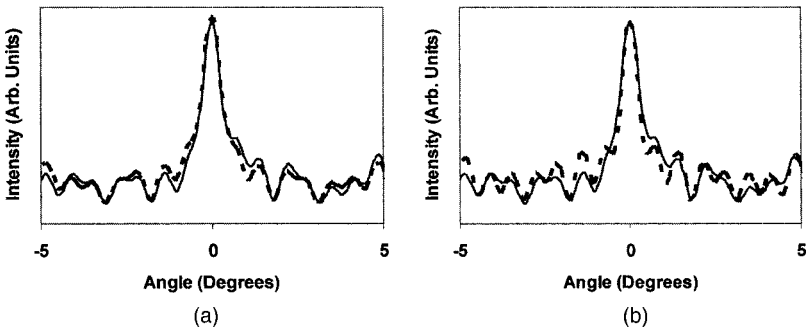

Fig. 13. (a) Comparison of the image of an ideal point source with constant amplitude (dashed curve) with the experimental data (solid curve). (b) Comparison of the experimental image (solid curve) with a theoretical image (dashed curve) where only a near-field correction to the phase has been applied, while the (nonconstant) amplitudes were used as measured.

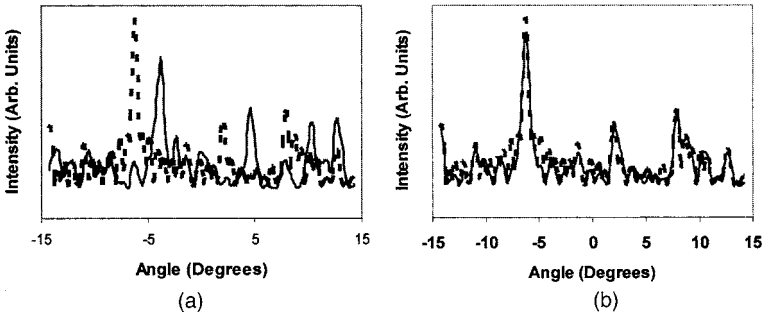

Fig. 14. (a) Comparison of a reconstructed line image (solid curve) without near-field correction and theoretical point image (dashed curve) for the data of Fig. 11. (b) Comparison of reconstructed line image (solid curve) including a near-field correction.

for stand-off detection, the reconstructed images must be corrected for near-field aberrations. Near-field corrections can be introduced either by arranging the detectors of the array into a circular pattern or by arranging the detectors such that they match the expected curvature of the incoming wavefronts. For the particular THz point source used, the near-field phase corrections have a stronger impact on the reconstructed image than amplitude corrections. The measured point-spread function corresponds well to theoretical predictions when near-field corrections are included. The dependence of the angular resolution on the THz wavelength and maximum baseline is verified.

ACKNOWLEDGMENTS

The authors gratefully acknowledge the support of the Technical Service Working Group, the Department of Homeland Security, and the U.S. Army Small Business Innovation Research contract (DAAD19-03-C-0038). Enlightening discussions with J. M. Joseph are gratefully acknowledged.

Corresponding author J. F. Federici may be reached at Department of Physics, New Jersey Institute of Technology, 323 King Boulevard, Newark, New Jersey 07102; by phone at 973-596-8482; or by e-mail at federici @adm.njit.edu.

REFERENCES

1. D. L. Woolard, W. R. Loerop, and M. Shur, eds., *Terahertz Sensing Technology, Vol. 2: Emerging Scientific Applications & Novel Device Concepts* (World Scientific, 2003).
2. D. Mittleman, ed., *Sensing with Terahertz Radiation* (Springer, 2003).
3. See for example J. F. Federici, B. Schulkin, F. Huang, D. Gary, R. Barat, F. Oliveira, and D. Zimdars, "THz imaging and sensing for security applications—explosives, weapons, and drugs," Semicond. Sci. Technol. **20**, S266–S280 (2005); http://stacks.iop.org/0268-1242/20/S266 and references therein.
4. B. B. Hu and M. C. Nuss, "Imaging with terahertz waves," Opt. Lett. **20**, 1716–1718 (1995).
5. D. M. Mittleman, S. Hunsche, L. Boivin, and M. C. Nuss, "T-ray tomography," Opt. Lett. **22**, 904–906 (1997).
6. D. A. Zimdars, "Fiber-pigtailed terahertz time-domain spectroscopy instrumentation for package inspection and security imaging," in Proc. SPIE **5070**, 108–116 (2003).
7. W. R. Tribe, D. A. Newnham, P. F. Taday, and M. C. Kemp, "Hidden object detection: security applications of terahertz technology," in Proc. SPIE **5354**, 168–176 (2004).
8. M. C. Kemp, P. F. Taday, B. E. Cole, J. A. Cluff, A. J. Fitzgerald, and W. R. Tribe, "Security applications of terahertz technology," in Proc. SPIE **5070**, 44–52 (2003).
9. D. Zimdars and J. S. White, "Terahertz reflection imaging for package and personnel inspection," in Proc. SPIE **5411**, 78–83 (2004).
10. C. A. Schuetz and D. W. Prather, "Optical upconversion techniques for high-sensitivity millimeter-wave detection," in Proc. SPIE **5619**, 166–174 (2004).
11. Q. Wu, T. D. Hewitt, and X. C. Zhang, "Two-dimensional electro-optic imaging of THz beams," Appl. Phys. Lett. **69**, 1026–1028 (1996).
12. Z. Jiang and X. C. Zhang, "Single-shot spatiotemporal terahertz field imaging," Opt. Lett. **23**, 1114–1116 (1998).
13. A. R. Thompson, J. M. Moran, and G. W. Swenson, *Interferometry and Synthesis in Radio Astronomy*, 2nd ed. (Wiley, 2001), p. 50.
14. K. McKlatchy, M. T. Reiten, and R. A. Cheville, "Time resolved synthetic aperture terahertz impulse imaging," Appl. Phys. Lett. **79**, 4485–4487 (2001).
15. A. B. Ruffin, J. Decker, L. Sanchez-Palencia, L. Le Hors, J. F. Whitaker, T. B. Norris, and J. V. Rudd, "Time reversal and object reconstruction with single-cycle pulses," Opt. Lett. **26**, 681–683 (2001).
16. T. D. Dorney, J. L. Johnson, J. Van Rudd, R. G. Baraniuk, W. W. Symes, and D. M. Mittleman, "Terahertz reflection imaging using Kirchhoff migration," Opt. Lett. **26**, 1513–1515 (2001).
17. J. O'Hara and D. Grischkowsky, "Quasi-optic terahertz imaging," Opt. Lett. **26**, 1918–1920 (2001).
18. J. O'Hara and D. Grischkowsky, "Synthetic phased-array terahertz imaging," Opt. Lett. **27**, 1070–1072 (2002).
19. J. O'Hara and D. Grischkowsky, "Quasi-optic synthetic phased-array terahertz imaging," J. Opt. Soc. Am. B **21**, 1178–1191 (2004).
20. D. H. Johnson and D. E. Dungeon, *Array Signal Processing* (Prentice Hall, 1993), pp. 114–115.
21. J. F. Federici, D. Gary, B. Schulkin, F. Huang, H. Altan, R. Barat, and D. Zimdars, "Terahertz imaging using an interferometric array," Appl. Phys. Lett. **83**, 2477–2479 (2003).
22. K. P. Walsh, B. Schulkin, D. Gary, J. F. Federici, R. Barat, and D. Zimdars, "Terahertz near-field interferometric and synthetic aperture imaging," in Proc. SPIE **5411**, 9–17 (2004).
23. M. Born and E. Wolf, *Principles of Optics*, 7th ed. (Cambridge U. Press, 1999), pp. 574–579.
24. K. A. McIntosh, E. R. Brown, K. B. Nichols, O. B. McMahon, W. F. DiNatale, and T. M. Lyszczarz, "Terahertz photomixing with diode lasers in low-temperature-grown GaAs," Appl. Phys. Lett. **67**, 3844–3846 (1995).
25. S. M. Duffy, S. Verghese, and K. A. McIntosh,"Photomixers for continuous-wave terahertz radiation," in *Sensing with Terahertz Radiation*, D. Mittleman, ed. (Springer, 2002).
26. T. L. J. Chan, J. E. Bjarnason, A. W. M. Lee, M. A. Celis, and E. R. Brown, "Attenuation contract between biomolecular and inorganic materials at terahertz frequencies," Appl. Phys. Lett. **85**, 2523–2525 (2004).
27. E. R. Brown, "Fundamentals of terrestrial millimeter-wave and THz remote sensing," in Ref. 1, pp. 93–96.
28. T. Loffler, K. J. Siebert, H. Quast, N. Hasegawa, G. Lota, R. Wipe, T. Hahn, M. Thomson, R. Leonhardt, and H. G. Roskos, "All-optoelectronic continuous-wave terahertz systems," Philos. Trans. R. Soc. London, Ser. A **362**, 263–265 (2004).
29. K. J. Siebert, T. Loffler, H. Quast, M. Thomason, T. Bauer, R. Leonhardt, S. Czasch, and H. G. Roskos, "All optoelectronic continuous wave THz imaging for biomedical applications," Phys. Med. Biol. **47**, 2743–2750 (2002).
30. K. J. Siebert, H. Quast, R. Leonhardt, T. Loffler, M. Thomson, T. Bauer, H. G. Roskos, and S. Czasch, "Continuous-wave all-optoelectronic terahertz imaging," Appl. Phys. Lett. **80**, 3003–3005 (2002).
31. T. Kleine-Ostmann, P. Knobloch, M. Koch, S. Hoffman, M. Breede, M. Hofmann, G. Hain, K. Pierz, M. Sperling, and K. Donhuijsen, "Continuous-wave THz imaging," Electron. Lett. **37**, 1461–1463 (2001).
32. I. S. Gregory, W. R. Tribe, B. E. Cole, C. Baker, M. J. Evans, I. V. Bradley, E. H. Linfiled, A. G. Davies, and M. Missous, "Phase sensitive continuous-wave THz imaging using diode lasers," Electron. Lett. **40**, 143–145 (2004).
33. J. E. Bjarnason, T. L. J. Chan, A. W. M. Lee, E. R. Brown, D. C. Driscoll, M. Hanson, A. C. Gassard, and R. E. Muller, "ErAs:GaAs photomixer with two-decade tunability and 12 μW peak output power," Appl. Phys. Lett. **85**, 3983–3985 (2004).
34. S. Verghese, K. A. McIntosh, and E. R. Brown, "Optical and terahertz power limits in the low-temperature-grown GaAs photomixers," Appl. Phys. Lett. **71**, 2743–2745 (1997).
35. V. Ryzhii, I. Khmyrova, and M. Shur, "Terahertz

photomixing in quantum well structures using resonant excitation of plasma oscillations," J. Appl. Phys. **91**, 1875–1881 (2002).
36. V. Ryzhii, I. Khmyrova, A. Satou, P. O. Vaccaro, T. Aida, and M. Shur, "Plasma mechanism of terahertz photomixing in high-electron mobility transistor under interband photoexcitation," J. Appl. Phys. **92**, 5756–5760 (2002).
37. A. Malcoci, A. Stohr, A. Sauerwald, S. Schulz, and D. Jager, "Waveguide and antenna coupled traveling-wave 1.55 μm photodetectors for optical (sub)millimeter-wave generation," in Proc. SPIE **5466**, 202–209 (2004).
38. A. Nahata, J. T. Yardley, and T. F. Heinz, "Two-dimensional imaging of continuous-wave terahertz radiation using electro-optic detection," Appl. Phys. Lett. **81**, 963–965 (2002).
39. J. Van Rudd and D. Mittleman, "Influence of substrate-lens design in terahertz time-domain spectroscopy," J. Opt. Soc. Am. B **19**, 319–329 (2002).
40. M. Tani, P. Gu, M. Hyodo, K. Saki, and T. Hidaka, "Generation of coherent terahertz radiation by photomixing of dual-mode lasers," Opt. Quantum Electron. **32**, 503–520 (2000).